Dynamics of Strongly Nonlinear Internal Solitary Waves in Shallow Water

By Tae-Chang Jo and Wooyoung Choi

We study the dynamics of large amplitude internal solitary waves in shallow water by using a strongly nonlinear long-wave model. We investigate higher order nonlinear effects on the evolution of solitary waves by comparing our numerical solutions of the model with weakly nonlinear solutions. We carry out the local stability analysis of solitary wave solution of the model and identify an instability mechanism of the Kelvin–Helmholtz type. With parameters in the stable range, we simulate the interaction of two solitary waves: both head-on and overtaking collisions. We also study the deformation of a solitary wave propagating over non-uniform topography and describe the process of disintegration in detail. Our numerical solutions unveil new dynamical behaviors of large amplitude internal solitary waves, to which any weakly nonlinear model is inapplicable.

1. Introduction

Under the assumption of small wave amplitude, various weakly nonlinear models have been proposed to describe the evolution of internal solitary waves. Different models under different approximations can be found, for example,

Address for correspondence: W. Choi, Department of Naval Architecture & Marine Engineering, University of Michigan, Ann Arbor, MI 48109-2145, USA. E-mail: wychoi@engin.umich.edu. This work was supported in part by the US Department of Energy. The authors thank R. Camassa, Y. Li, and H. Klisch for their helpful remarks.

Published by Blackwell Publishing, 350 Main Street, Malden, MA 02148, USA, and 108 Cowley Road, Oxford, OX4 1JF, UK.

in Choi and Camassa [1]. However, there have been an increasing number of observations of large amplitude internal solitary waves [2], for which the classical weakly nonlinear assumption is no longer valid.

For both shallow and deep water configurations, Choi and Camassa [3] recently derived a new model for strongly nonlinear long waves in a simple two-layer system. They used a systematic asymptotic expansion method for a natural small parameter in the ocean, that is, the aspect ratio between vertical and horizontal length scales. The most prominent feature of large amplitude solitary waves of the model is that they are much wider and slower compared with weakly nonlinear solitary waves described by the Kortweg–de Vries (KdV) and Intermediate Long Wave (ILW) equations for the shallow and deep water configurations, respectively.

Although steady solitary wave solutions of the model are in excellent agreement with numerical solutions of the Euler equations and experimental data [4], little is known about their dynamical properties. Due to their complexity, it is very difficult to study the dynamics of large amplitude internal waves in detail by using the original governing (Euler) equations and the boundary conditions. Here, by taking advantage of simplicity of the model, we investigate the evolution of large amplitude internal solitary waves in the shallow water configuration.

This paper is organized as follows. With the model described in Section 2, we present the local stability analysis of solitary wave solution of the model in Section 3, by assuming that a slowly varying flow field generated by interfacial solitary wave can be regarded as locally constant. In Section 4, after choosing physical parameters appropriate for numerical stability, we study the interaction between two solitary waves: the head-on and overtaking collisions. Because phase shift is a typical nonlinear phenomenon occurring during the interaction, we numerically measure phase shift to compare with weakly nonlinear result. In Section 5, we also study the evolution of a solitary wave propagating over non-uniform topography. The process of fission is described in detail and the number of solitary waves disintegrated from one solitary wave is compared with weakly nonlinear prediction.

2. Mathematical models

2.1. Strongly nonlinear model

To describe the evolution of large amplitude internal gravity waves, Choi and Camassa [3] proposed a strongly nonlinear model for a two-layer system with flat top and bottom boundaries. With non-uniform bottom topography (as shown in Figure 1), the model needs to be slightly modified [5] and can be written as

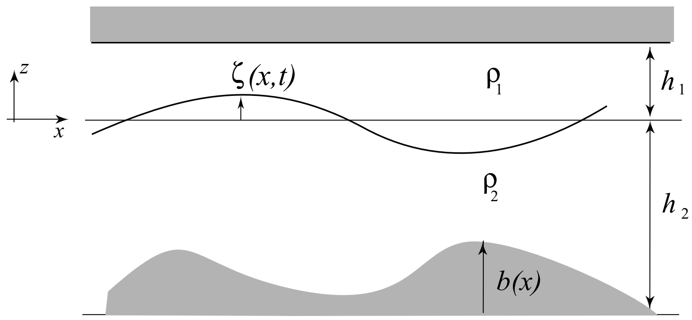

Figure 1. Two-layer system.

$$\eta_{1t} + (\eta_1 \bar{u}_1)_x = 0, \qquad \eta_{2t} + (\eta_2 \bar{u}_2)_x = 0, \tag{1}$$

$$\bar{u}_{1t} + \bar{u}_1 \bar{u}_{1x} + g\zeta_x = -\frac{P_x}{\rho_1} + \frac{1}{\eta_1}\left(\frac{1}{3}\eta_1^3 G_1\right)_x, \tag{2}$$

$$\bar{u}_{2t} + \bar{u}_2 \bar{u}_{2x} + g\zeta_x = -\frac{P_x}{\rho_2} + \frac{1}{\eta_2}\left(\frac{1}{3}\eta_2^3 G_2\right)_x + \frac{1}{\eta_2}\left(\frac{1}{2}\eta_2^2 H_2\right)_x + \left(\frac{1}{2}\eta_2 G_2 + H_2\right) b'(x), \tag{3}$$

where g is the gravitational acceleration, ρ_i is the fluid density, and the subscripts x and t represent partial differentiation with respect to space and time, respectively. In (1)–(3), the layer thickness η_i, the thickness average velocity $\bar{u}_i$, and the nonlinear dispersive term G_i are defined by

$$\eta_1 = h_1 - \zeta, \quad \bar{u}_1(x,t) = \frac{1}{\eta_1}\int_{\zeta}^{h_1} u_1(x,z,t)\,dz, \quad G_1(x,t) = \bar{u}_{1xt} + \bar{u}_1\bar{u}_{1xx} - (\bar{u}_{1x})^2, \tag{4}$$

$$\eta_2 = h_2 - b(x) + \zeta, \quad \bar{u}_2(x,t) = \frac{1}{\eta_2}\int_{-h_2+b(x)}^{\zeta} u_2(x,z,t)\,dz, \quad G_2(x,t) = \bar{u}_{2xt} + \bar{u}_2\bar{u}_{2xx} - (\bar{u}_{2x})^2, \tag{5}$$

and H_2 is given by

$$H_2 = -(\partial_t + \bar{u}_2\partial_x)(\bar{u}_2 b_x). \tag{6}$$

While the first two equations in (1) representing conservation of mass are exact, two horizontal momentum equations, (2)–(3), have an error of $O(\epsilon^4)$, where ϵ measuring the ratio between water depth and characteristic wavelength has been assumed to be small. Because no assumption on wave amplitude has been made, this model is expected to describe the evolution of large amplitude internal waves much better than any weakly nonlinear models based on small amplitude assumption. The bottom topography $b(x)$ is also assumed to be slowly varying and we recover the system of equations derived by Choi and Camassa [3] when $b(x) = 0$.

The system of equations (1)–(3) can be further reduced to two evolution equations. From (1), by imposing zero boundary conditions at both infinities, $\bar{u}_2$ can be expressed, in terms of $\bar{u}_1$, as

$$\bar{u}_2 = -\left(\frac{\eta_1}{\eta_2}\right)\bar{u}_1. \tag{7}$$

After eliminating P_x from (2)–(3) and using (7) for the expression of $\bar{u}_2$, one can find a closed system of two evolution equations for η_1 and $\bar{u}_1$.

2.2. *Weakly nonlinear models*

Assuming $\zeta = O(\bar{u}_1) = O(\bar{u}_2) \ll 1$, the system of (1)–(3) can be reduced to the weakly nonlinear model, written for ζ and $\bar{u}_1$, as

$$\zeta_t - [(h_1 - \zeta)\bar{u}_1]_x = 0, \tag{8}$$

$$\bar{u}_{1t} + q_1\bar{u}_1\bar{u}_{1x} + (q_2 + q_3\zeta)\zeta_x = q_4\bar{u}_{1xxt}, \tag{9}$$

where q_is are slowly varying functions defined by

$$q_1 = \frac{\rho_1\hat{h}_2^2 - \rho_2 h_1\hat{h}_2 - 2\rho_2 h_1^2}{\hat{h}_2(\rho_1\hat{h}_2 + \rho_2 h_1)}, \qquad q_2 = \frac{g\hat{h}_2(\rho_1 - \rho_2)}{\rho_1\hat{h}_2 + \rho_2 h_1}, \tag{10}$$

$$q_3 = \frac{g\rho_2(\rho_1 - \rho_2)(h_1 + \hat{h}_2)}{(\rho_1\hat{h}_2 + \rho_2 h_1)^2}, \qquad q_4 = \frac{1}{3}\frac{h_1\hat{h}_2(\rho_1 h_1 + \rho_2\hat{h}_2)}{\rho_1\hat{h}_2 + \rho_2 h_1}, \tag{11}$$

and $\hat{h}_2(x) = h_2 - b(x)$. The system of equations (8)–(9) will be used for weakly nonlinear analyses presented in Sections 4 and 5.

For unidirectional waves, the system (8)–(9) with $b(x) = 0$ can be further reduced to the Korteweg–de Vries equation for $\zeta(x, t)$ given by

$$\zeta_t + c_0\zeta_x + c_1\zeta\zeta_x + c_2\zeta_{xxx} = 0, \tag{12}$$

where

$$c_0^2 = \frac{gh_1h_2(\rho_2 - \rho_1)}{\rho_1 h_2 + \rho_2 h_1}, \quad c_1 = \frac{q_2}{2c_0}\left(2 + q_1 - \frac{q_3 h_1}{q_2}\right), \quad c_2 = \frac{1}{2}q_4 c_0. \tag{13}$$

3. Solitary waves and their stability

3.1. Solitary waves

By assuming solitary wave of speed c to have the form of

$$\zeta(x,t) = \zeta(X), \qquad \bar{u}_i(x,t) = \bar{u}_i(X), \quad X = x - ct, \tag{14}$$

and imposing the boundary condition of $\eta_i \to h_i$ as $|X| \to \infty$, $\bar{u}_i$ can be written, from (1), as

$$\bar{u}_i = c\left(1 - \frac{h_i}{\eta_i}\right). \tag{15}$$

As shown in [3], by using (15), the strongly nonlinear model (2)–(3) for $b(x) = 0$ becomes

$$(\zeta_X)^2 = \left[\frac{3g(\rho_2 - \rho_1)}{c^2\left(\rho_1 h_1^2 - \rho_2 h_2^2\right)}\right]\frac{\zeta^2(\zeta - a_-)(\zeta - a_+)}{(\zeta - a_*)}, \tag{16}$$

where a_* is given by

$$a_* = -\frac{h_1 h_2(\rho_1 h_1 + \rho_2 h_2)}{\rho_1 h_1^2 - \rho_2 h_2^2}, \tag{17}$$

and $a_\pm$ are the two roots of a quadratic equation

$$\zeta^2 + d_1\zeta + d_2 = 0, \tag{18}$$

with d_1 and d_2 defined by

$$d_1 = -\frac{c^2}{g} - h_1 + h_2, \quad d_2 = h_1 h_2\left(\frac{c^2}{c_0^2} - 1\right). \tag{19}$$

From the fact that ζ is bounded and ${\zeta_X}^2$ is non-negative, it can be shown that the solitary wave can be of elevation for $(h_2/h_1) < (\rho_2/\rho_1)^{1/2}$ and of depression for $(h_2/h_1) > (\rho_2/\rho_1)^{1/2}$. Notice that no solitary wave solution exists at the critical depth ratio given by $(h_2/h_1) = (\rho_2/\rho_1)^{1/2}$. From (18), the solitary wave speed c can be written in terms of wave amplitude a as

$$\frac{c^2}{c_0^2} = \frac{(h_1 - a)(h_2 + a)}{h_1 h_2 - \left(c_0^2/g\right)a}. \tag{20}$$

The solitary wave profiles of the strongly nonlinear model are shown in Figure 2(a). As wave amplitude increases, the solitary wave of the strongly nonlinear model becomes much wider and slower than those of weakly nonlinear models as shown in [3].

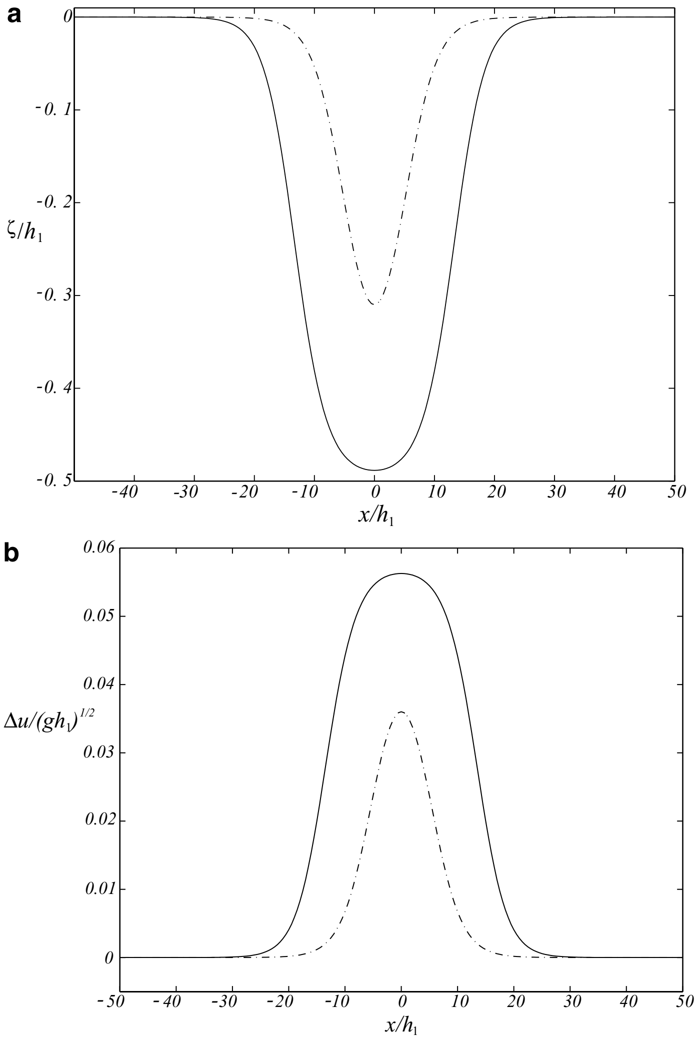

Figure 2. (*a*) Solitary wave profiles with amplitude $a = -0.31$ (— - —) and $a = -0.4885$ (———) for $\rho_2/\rho_1 = 1.01$ and $h_2/h_1 = 2$, (*b*) the velocity jump, Δu, given by (21) for solitary waves shown in (*a*).

From (15), notice that the interfacial solitary wave induces the horizontal velocity discontinuity across the interface given by

$$\Delta u \equiv \bar{u}_1 - \bar{u}_2 = -c\zeta\left(\frac{1}{h_1 - \zeta} + \frac{1}{h_2 + \zeta}\right). \tag{21}$$

Although this discontinuity vanishes at both infinities, it reaches the maximum at the peak as shown in Figure 2(*b*), which may be large enough to excite the

Kelvin–Helmholtz-type instability. Because disturbances with small wavelength are most dangerous in this instability mechanism [6], the slowly varying velocity jump in (21) can be regarded as locally constant. Although a stability analysis for non-uniform flow field induced by the solitary wave is a very interesting problem, it is beyond the scope of this article and the local stability analysis for a constant basic state is sufficient to determine the onset of instability of solitary wave.

3.2. Local stability analysis

We consider small perturbations (u_i', ζ') to a basic state as

$$\bar{u}_i = u_i + u_i', \qquad \zeta = a + \zeta', \tag{22}$$

where u_i and a are constant.

We first study the case of $a = 0$ and $\Delta u \neq 0$ to understand the Kelvin–Helmholtz instability of the system. For the instability of solitary wave, we later consider the case of $a \neq 0$ for which Δu is a function of a given by (21).

By substituting (22) with $a = 0$ into (1)–(3) and linearizing with respect to (u_i', ζ'), we can find the linear dispersion relation between wavenumber k and wave frequency ω for a Fourier mode of $e^{i(kx-\omega t)}$ as

$$a(\bar{k})\bar{\omega}^2 - 2b(\bar{k})\bar{\omega} + c(\bar{k}) = 0, \tag{23}$$

where $\bar{k} = kh_1$, $\bar{\omega} = \omega/\sqrt{g/h_1}$, and

$$\begin{aligned} a(\bar{k}) &= h(1 + \rho h)\bar{k}^2 + 3(h + \rho), \\ b(\bar{k}) &= \frac{u_1}{\sqrt{gh_1}}[h(1 + \rho hu)\bar{k}^3 + 3(h + \rho u)\bar{k}], \\ c(\bar{k}) &= \frac{u_1^2}{gh_1}[h(1 + \rho hu^2)\bar{k}^4 + 3(\rho u^2 + h)\bar{k}^2] - 3h(\rho - 1)\bar{k}^2, \end{aligned} \tag{24}$$

where the depth ratio h, the density ratio ρ, and the Froude number F are defined as

$$h = h_2/h_1, \quad \rho = \rho_2/\rho_1, \quad u = u_2/u_1, \quad F = (u_2 - u_1)/\sqrt{gh_1}. \tag{25}$$

A constant state becomes unstable when there exists a non-trivial imaginary part of ω, in other words, when $\Delta(\bar{k}, F) > 0$ for fixed ρ and h, where

$$\begin{aligned} D(\bar{k}, F) = (\rho h^3 F^2)\bar{k}^4 &- 3[h^2(\rho - 1)(1 + \rho h) - h(1 + h^2)\rho F^2]\bar{k}^2 \\ &- 9[h(h + \rho)(\rho - 1) - \rho h F^2]. \end{aligned} \tag{26}$$

It is interesting to compare the linear dispersion relation (23) from the longwave model (1)–(3) with that for the full linear problem. When we perturb the Euler equations about (22), ω is still determined by (23) with $a(\bar{k})$, $b(\bar{k})$, and $c(\bar{k})$ replaced by

$$\begin{aligned} a(\bar{k}) &= \left[\frac{\rho}{\bar{k}\tanh(h\bar{k})} + \frac{1}{\bar{k}\tanh(\bar{k})}\right], \\ b(\bar{k}) &= \frac{u_1}{\sqrt{gh_1}}\left[\frac{\rho u}{\tanh(h\bar{k})} + \frac{1}{\tanh(\bar{k})}\right], \\ c(\bar{k}) &= \frac{u_1^2}{gh_1}\left[\frac{\rho\bar{k}u^2}{\tanh(h\bar{k})} + \frac{1}{\tanh(\bar{k})}\right] + \rho - 1. \end{aligned} \tag{27}$$

Then $D(\bar{k}, F)$ is given, instead of (26), by

$$D(\bar{k}, F) = \frac{F^2\rho}{\tanh(h\bar{k})\tanh(\bar{k})} - (\rho - 1)\left[\frac{\rho}{\bar{k}\tanh(h\bar{k})} + \frac{1}{\bar{k}\tanh(\bar{k})}\right]. \tag{28}$$

As shown in Figure 3(a), the constant state of the model, (22), is unstable for large k corresponding to small wavelength and relatively stable for small k. Because the constant state becomes unstable for high wavenumbers for any Froude number, the strongly nonlinear system of (1)–(3) is ill-posed. For fixed Froude number F, only perturbations with small wavenumbers are stable.

As expected from the fact that (27) is valid for arbitrary wavelength, it can be shown that (24) can be obtained by expanding (27) for small $\bar{k}$. On the other hand, as wavenumber $\bar{k}$ increases, the critical Froude number from the model decreases like $O(\bar{k}^{-2})$, while that of the linear Euler equations decreases like $O(\bar{k}^{-1/2})$.

The stability diagram depends more on the density ratio than the depth ratio as shown in Figure 3(b). When we double the density ratio, the range of stable region becomes much wider but it changes little with doubling the depth ratio. This result can be understood from the fact that increasing the density ratio stabilizes the system.

To examine the instability of solitary wave, we need to extend our analysis for $a = 0$ to the case of non-zero a. To do this, we simply need to replace h_1 and h_2 in (26) by $h_1 - a$ and $h_2 + a$, respectively. Then wave amplitude a is the only free parameter because, from (21), the maximum velocity jump (and the Froude number) depends only on a as shown in Figure 4(a). Our local stability analysis is compared with the stability of our numerical code in Figure 4(b) with wavenumber k defined by $k = 2\pi/(2\Delta x)$. Notice that our numerical code becomes unstable near the neutral stability curve predicted by the local analysis. This confirms the validity of our local analysis and numerical code.

Given the fact that the strongly nonlinear model, (1)–(3), is linearly unstable for higher wave modes, we cannot test the convergence of our numerical solutions for very small grid size. To test the accuracy of our numerical code,

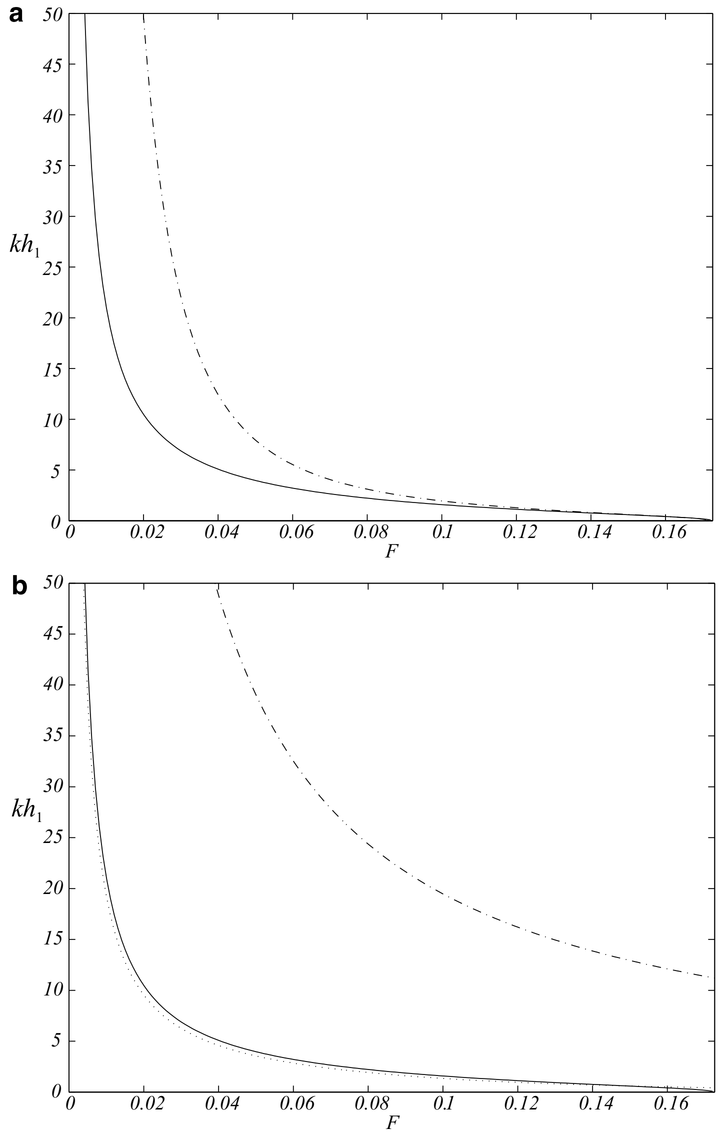

Figure 3. Neutral stability curve of $\Delta(\bar{k}, F) = 0$ between the Froude number F and wave number $\bar{k} = kh_1$: (a) the local analysis (——) given by (26) and the Kelvin–Helmholtz instability (—-—) given by (28) with $\rho_2/\rho_1 = 1.01$ and $h_2/h_1 = 2$, (b) the local stability analysis given by (26) for three different density and depth ratios: $\rho_2/\rho_1 = 1.01$ and $h_2/h_1 = 2$ (—); $\rho_2/\rho_1 = 1.01$ and $h_2/h_1 = 4$ ($\cdots$); $\rho_2/\rho_1 = 2.02$ and $h_2/h_1 = 2$ (—-—).

we calculate the error e with varying grid size, where e is defined as

$$e = \left(\frac{1}{N} \sum |\zeta - \zeta_{\text{exact}}|^2 \right)^{\frac{1}{2}}, \tag{29}$$

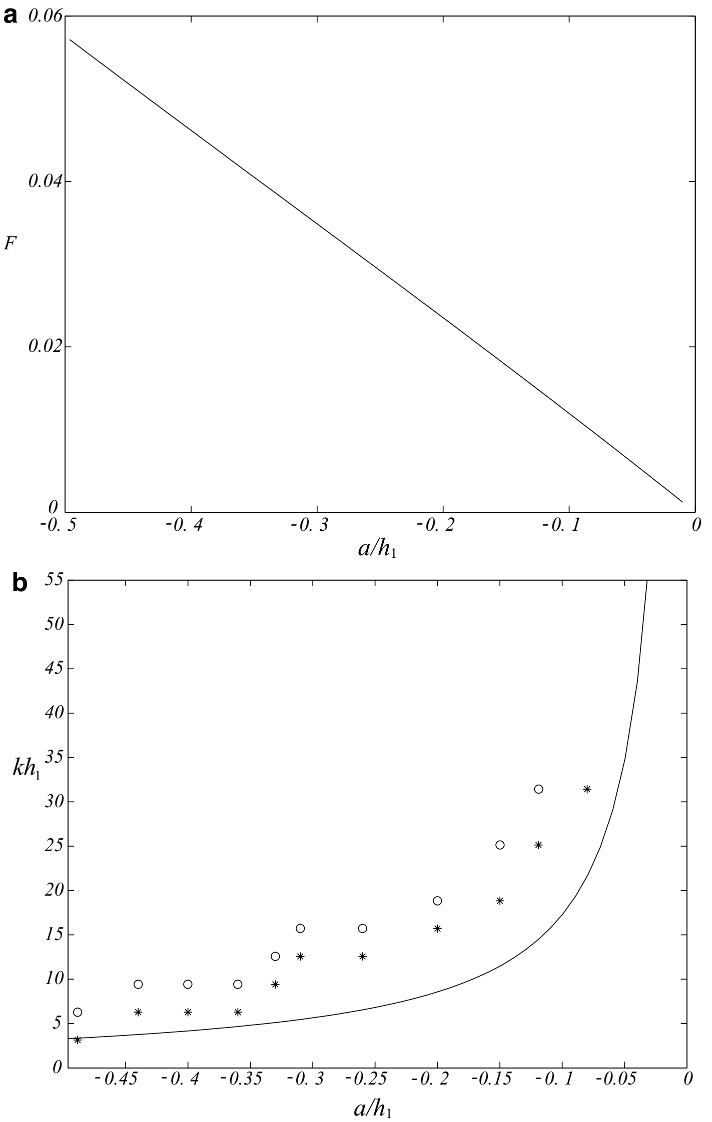

Figure 4. (*a*) Froude number versus wave amplitude, (*b*) neutral stability curve for the model (—) compared with numerically stable ($*$) and numerically unstable (o) solutions with $\rho_2/\rho_1 = 1.01$ and $h_2/h_1 = 2$.

where ζ_{exact} is the solution of (16). As shown in Table 1, e becomes smaller as the grid size Δx decreases, but the numerical code becomes unstable when Δx is too small, as expected.

For given Δx, solitary wave becomes stable or unstable depending on wave amplitude. For example, solitary wave with $a = -0.4885$ is unstable, while smaller solitary waves are stable, as shown in Figure 5.

Table 1
Comparison between Exact Solitary Wave Solutions and Numerical Solutions of the Model Given by (1)–(3) with Varying Grid Size

Δx	amp $= -0.08$	amp $= -0.15$	amp $= -0.31$
1.0	8.87E−05	2.72E−04	4.46E−04
0.5	4.21E−05	1.27E−04	9.98E−05
0.25	3.18E−05	9.31E−05	Unstable
0.125	2.87E−05	Unstable	Unstable
0.0625	Unstable	Unstable	Unstable

For numerical simulations presented in the following sections, we choose Δx being as small as possible, for which our code runs stably.

4. Interactions between two solitary waves

To identify higher order nonlinear effects present in the model on the evolution of large amplitude waves, we simulate the head-on and overtaking collisions between two solitary waves and compare our numerical solutions of the model with weakly nonlinear solutions.

4.1. Overtaking collision

When a larger solitary wave overtakes a smaller wave propagating in the same direction, it is well-known, from the KdV theory [7], that two weakly nonlinear solitary waves emerging after the collision remain unchanged in form. The larger wave experiences a forward phase shift, while the smaller wave shifts backward.

For a fixed amplitude ratio, the phase shift is known to be inversely proportional to $\sqrt{a_i}$ as

$$\Delta x_1 = -\frac{1}{\gamma_1}\log\left(\frac{\gamma_2+\gamma_1}{\gamma_2-\gamma_1}\right)^2, \quad \Delta x_2 = \frac{1}{\gamma_2}\log\left(\frac{\gamma_2+\gamma_1}{\gamma_2-\gamma_1}\right)^2, \quad \gamma_i^2 = \frac{c_1}{3c_2}a_i, \tag{30}$$

where a_i $(i = 1, 2)$ is the wave amplitude with $a_2 > a_1$ $(\gamma_2 > \gamma_1 > 0)$, and Δx_1 and Δx_2 are the phase shifts for smaller and larger waves, respectively.

For two different amplitude ratios, numerical solutions of our model are compared with weakly nonlinear solutions. For large amplitude ratio, the larger solitary wave takes over the smaller wave as shown in Figure 6 but, for small amplitude ratio, two waves just change their roles as shown in Figure 7. A similar observation has been made for weakly nonlinear waves based on the KdV theory [8].

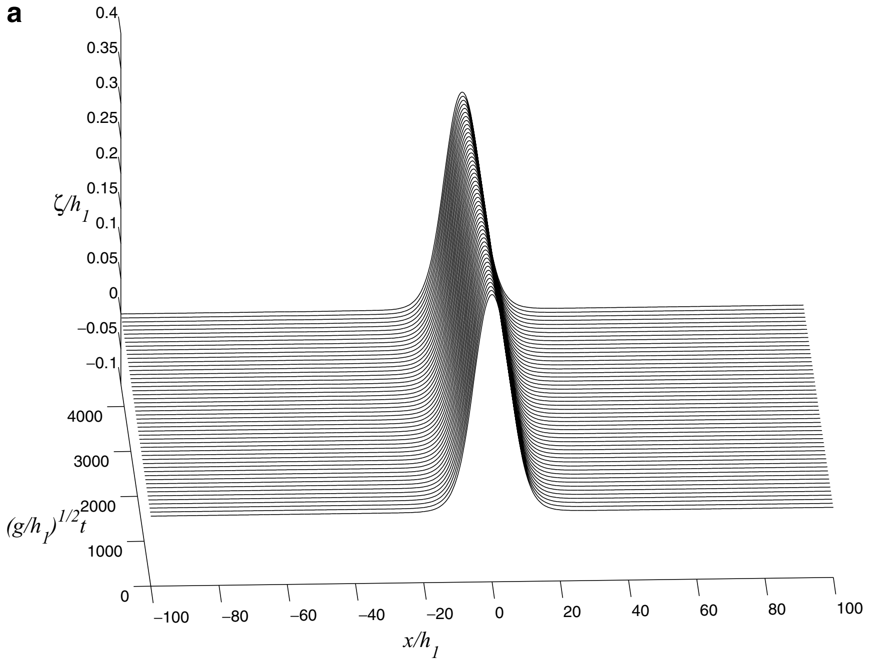

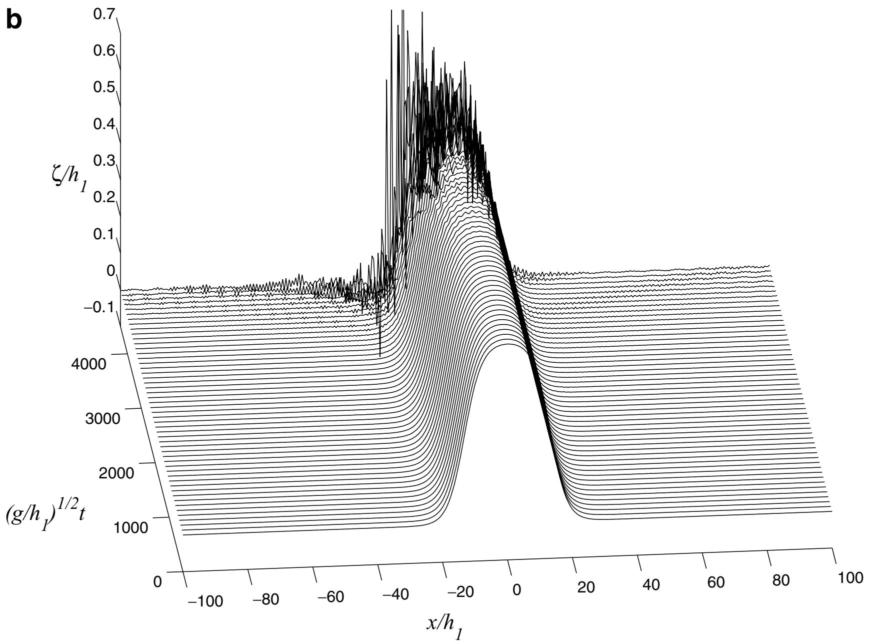

Figure 5. Numerical solutions for a solitary wave for $h_2/h_1 = 2$ and $\rho_2/\rho_1 = 1.01$ in a frame moving with solitary wave speed: (*a*) stable solitary wave of amplitude $a = -0.31$, (*b*) unstable solitary wave of amplitude $a = -0.4885$.

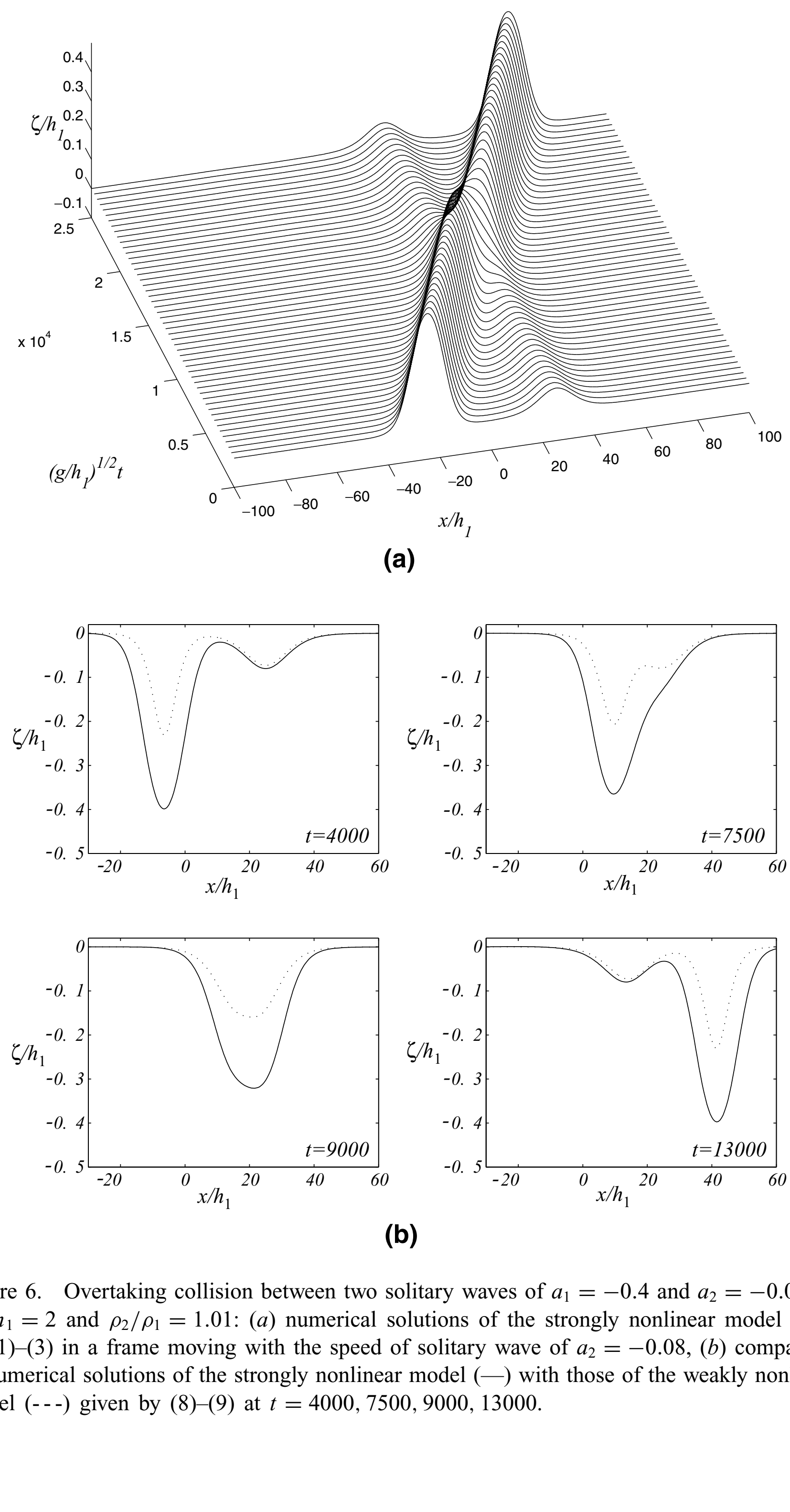

Figure 6. Overtaking collision between two solitary waves of $a_1 = -0.4$ and $a_2 = -0.08$ for $h_2/h_1 = 2$ and $\rho_2/\rho_1 = 1.01$: (*a*) numerical solutions of the strongly nonlinear model given by (1)–(3) in a frame moving with the speed of solitary wave of $a_2 = -0.08$, (*b*) comparison of numerical solutions of the strongly nonlinear model (—) with those of the weakly nonlinear model (- - -) given by (8)–(9) at $t = 4000, 7500, 9000, 13000$.

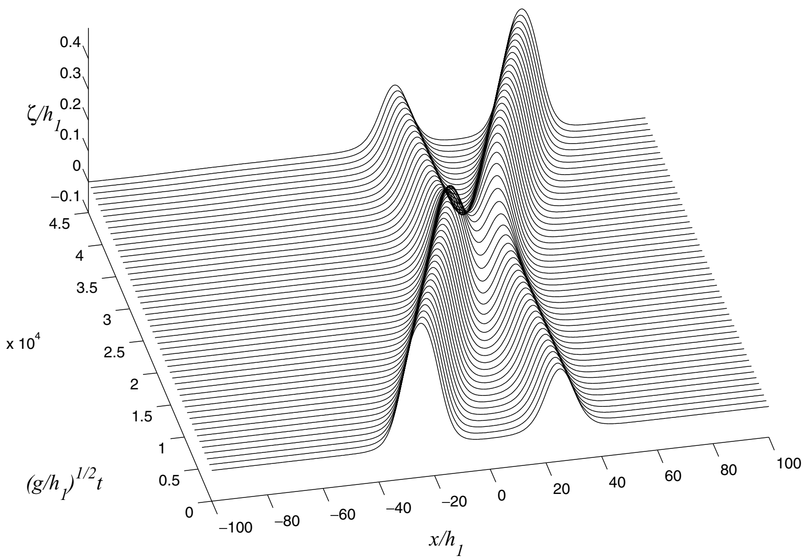

(a)

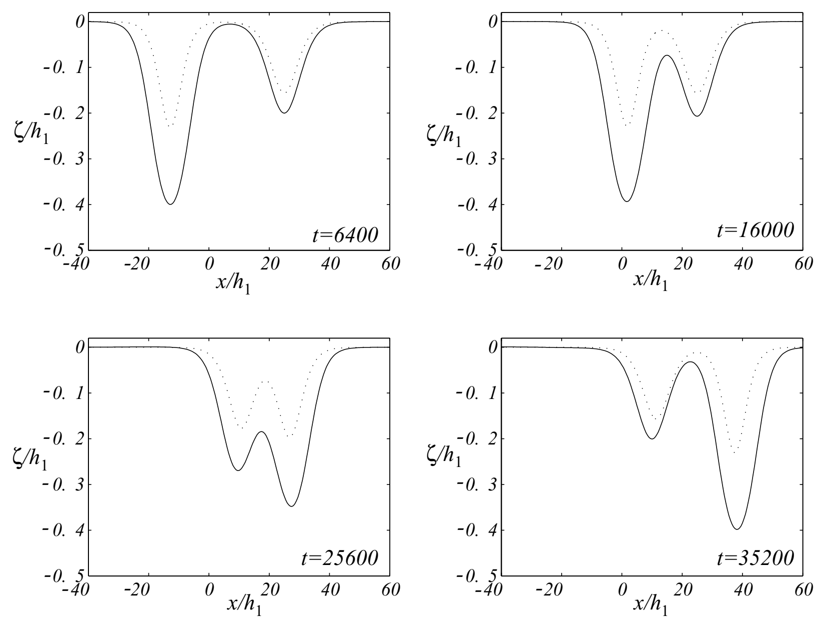

(b)

Figure 7. Overtaking collision between two solitary waves of $a_1 = -0.4$ and $a_2 = -0.2$ with $h_2/h_1 = 2$ and $\rho_2/\rho_1 = 1.01$: (*a*) numerical solutions of the strongly nonlinear model given by (1)–(3) in a frame moving with the speed of solitary wave of $a_2 = -0.2$, (*b*) comparison of numerical solutions of the strongly nonlinear model (—) with those of the weakly nonlinear model (- - -) given by (8)–(9) at $t = 6400$, 16000, 25600, 35200.

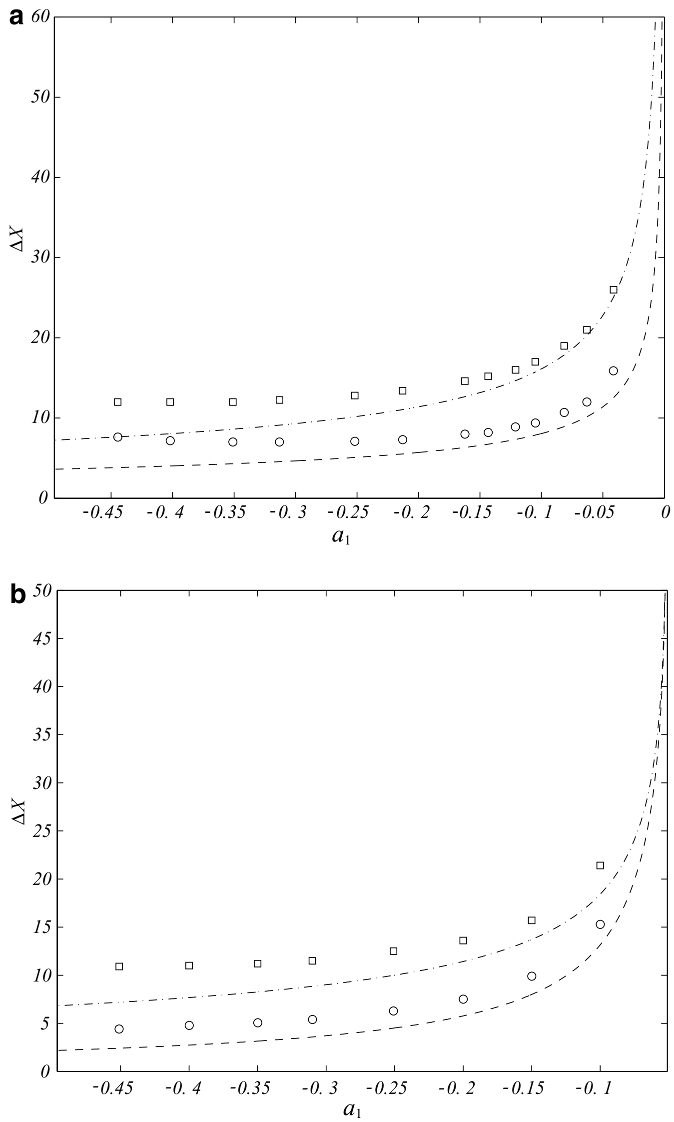

Figure 8. Phase shift after the overtaking collision between two solitary waves with $h_2/h_1 = 2$ and $\rho_2/\rho_1 = 1.01$. Numerical solutions of the strongly nonlinear solitary model (symbols) are compared with the weakly nonlinear analysis (—-—) given by (30): (*a*) the amplitude ratio is fixed as $a_1/a_2 = 4$, (*b*) the amplitude of the smaller wave is fixed as $a_2 = -0.051$.

In Figure 8, we compare phase shift measured from our numerical solutions with the weakly nonlinear prediction given by (30). While two results agree well for small wave amplitude, the phase shift is almost constant for large wave amplitude, which cannot be explained by the weakly nonlinear theory.

4.2. Head-on collision

Because the weakly nonlinear model for internal waves given by (8)–(9) is similar to the Boussinesq equations for surface waves except a term of $\zeta\zeta_x$ in (9), the weakly nonlinear analysis of Wu [8] for the head-on collision of two solitary waves at the free surface can be adopted here.

After introducing the slow variables $(\xi_\pm, \tau)$ defined by

$$\xi_\pm = \epsilon^{1/2}(x \mp c_0 t), \qquad \tau = \epsilon^{3/2} t, \tag{31}$$

for $\epsilon \ll 1$, we substitute into (8)–(9) the following expansion for $f = (\zeta, \bar{u}_1)$,

$$f = \epsilon f_1 + \epsilon^2 f_2 + O(\epsilon^3). \tag{32}$$

After collecting terms of $O(\epsilon)$, one can show that ζ_1 can be decomposed into the right- and left-going waves

$$\zeta_1 = \zeta_+(\xi_+, \tau) + \zeta_-(\xi_-, \tau), \tag{33}$$

where $\zeta_\pm(\xi_\pm, \tau)$ is governed by the KdV equation in the form of

$$\partial_\tau \zeta_\pm \pm c_1 \zeta_\pm \partial_\pm \zeta_\pm \pm c_2 \partial_\pm^3 \zeta_\pm = 0, \qquad \partial_\tau = \frac{\partial}{\partial \tau}, \quad \partial_\pm = \frac{\partial}{\partial \xi_\pm}. \tag{34}$$

The solitary wave solution of (34) is given by

$$\zeta_\pm = a_\pm \mathrm{sech}^2 \theta_\pm, \qquad \theta_\pm = \sqrt{\frac{c_1 a_\pm}{12 c_2}} \left(\xi_\pm - \frac{c_1}{3} a_\pm \tau - s_\pm \right). \tag{35}$$

At $O(\epsilon^2)$, ζ_2 representing the nonlinear interaction between two counter-propagating waves is found to be

$$\zeta_2 = \alpha \zeta_+ \zeta_- + \beta(\phi_- \partial_+ \zeta_+ - \phi_- \partial_- \zeta_-), \tag{36}$$

where α, β, and $\phi_\pm$ are defined as

$$\alpha = -\frac{q_1 + q_3 h_1/q_2}{2h_1}, \qquad \beta = -\frac{q_1 + q_3 h_1/q_2}{4c_0}, \qquad \partial_\pm \phi_\pm = \mp \sqrt{\frac{-q_2}{h_1}} \zeta_\pm. \tag{37}$$

From (32), (33) and (36), ζ can be rewritten, correct up to $O(\epsilon^2)$, as

$$\zeta = \zeta_+(\xi_+ + \beta\phi_-, \tau) + \zeta_-(\xi_- - \beta\phi_+, \tau) + \alpha \zeta_+(\xi_+, \tau) \zeta_-(\xi_-, \tau) + O(\epsilon^3), \tag{38}$$

and the phase shift can be computed as

$$\Delta x_\pm = \mp \beta [\phi_\mp(t = \infty) - \phi_\mp(t = -\infty)] = \pm \frac{2\beta q_2 a_\mp}{c_0} \sqrt{\frac{12 c_2}{c_1 a_\mp}}. \tag{39}$$

As shown in Figure 9, there is little difference in phase shift between our numerical solutions of the strongly nonlinear model and the weakly nonlinear

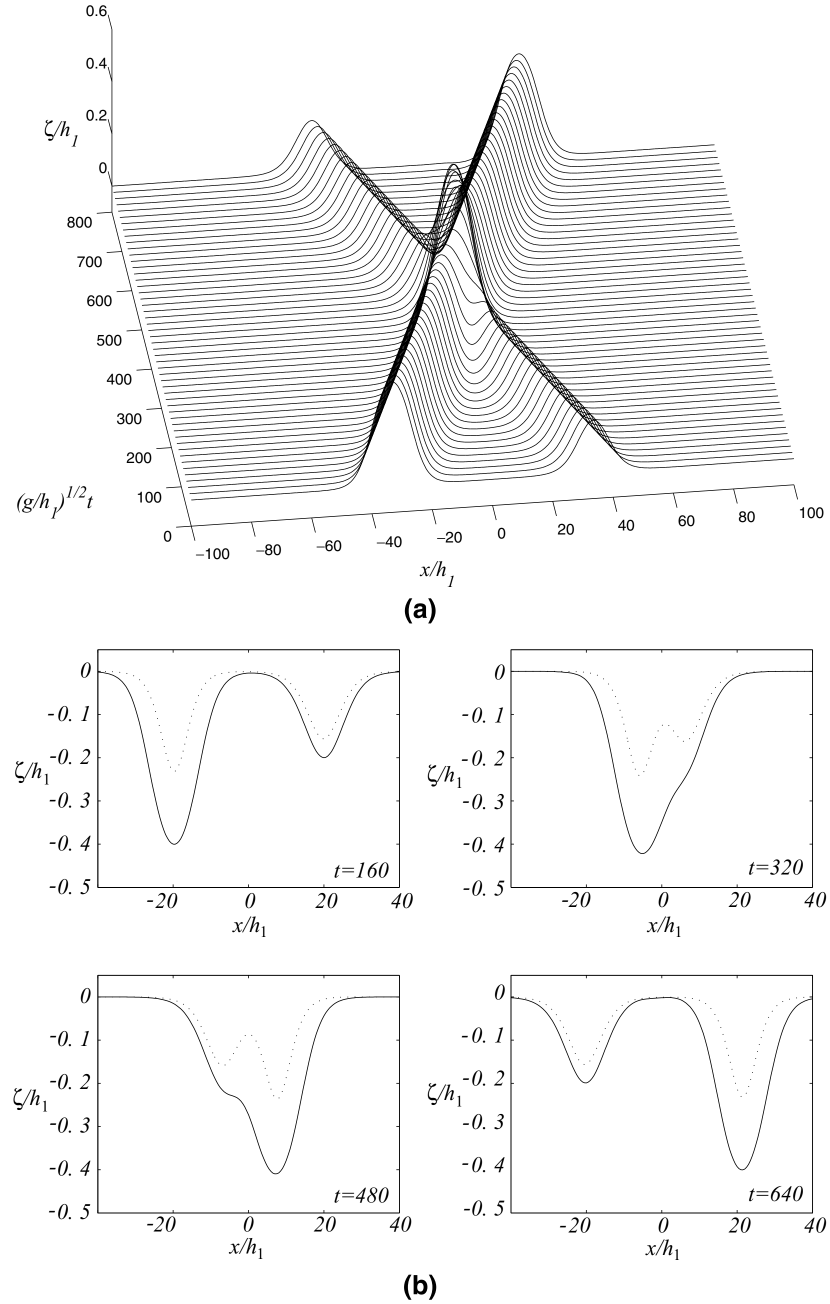

Figure 9. Head-on collision between two counter-propagating solitary waves of $a_1 = -0.4$ (for the right-going wave) and $a_2 = -0.2$ (for the left-going wave) for $h_2/h_1 = 2$ and $\rho_2/\rho_1 = 1.01$: (*a*) numerical solutions of the strongly nonlinear model given by (1)–(3), (*b*) comparison of numerical solutions of the strongly (—) and weakly (- - -) nonlinear models at $t = 160$, 320, 480, 640.

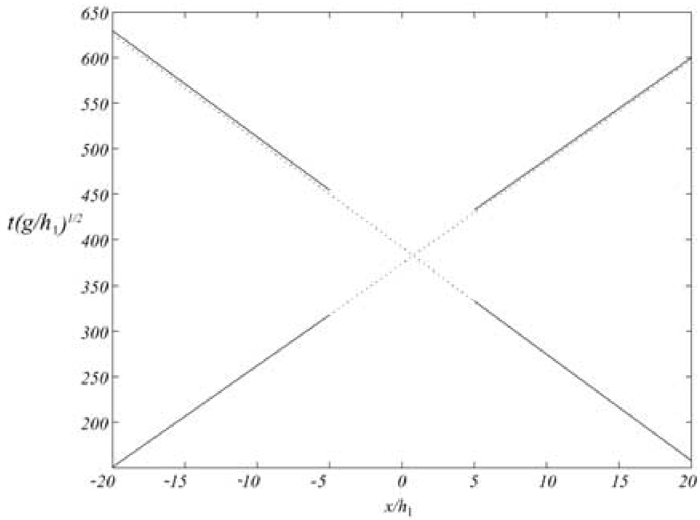

Figure 10. Peak location versus time for the head-on collision shown in Figure 9. Dotted lines represent the peak location without interaction.

analysis given by (39). Because two solitary waves move to the opposite directions, their interaction time is much shorter than that for the overtaking collision, yielding too small phase shift to measure accurately, as shown in Figure 10.

5. Evolution over non-uniform topography

Before presenting numerical solutions of the strongly nonlinear model, we briefly summarize the weakly nonlinear analysis.

For slowly varying bottom topography $\hat{h}_2(x) = h_2 - b(x)$, the weakly nonlinear model (8)–(9) can be reduced to the KdV equation with variable coefficients for ζ as shown by Djordjevic and Redekopp [9]:

$$\zeta_t + c_0(x)\zeta_x + c_1(x)\zeta\zeta_x + c_2(x)\zeta_{xxx} + \tfrac{1}{2}c_0'(x)\zeta = 0, \tag{40}$$

where the coefficients are given by (13) replacing h_2 by $\hat{h}_2$ and we have assumed that $\hat{h}_2'(x) = O(\epsilon^{3/2})$. By introducing the following stretched coordinates:

$$\xi = \epsilon^{1/2}\left(\int^x \frac{d\sigma}{c_0(\sigma)} - t\right), \qquad X = \epsilon^{3/2}\int^x \frac{c_2(x)}{[c_0(x)]^4}\,dx, \tag{41}$$

and making the following transformation for ζ

$$\zeta = -\frac{6c_2}{c_1 c_0^2}\psi(X,\xi), \tag{42}$$

we can show, from (40), that ψ satisfies

$$\psi_X - 6\psi\psi_\xi + \psi_{\xi\xi\xi} + \nu(X)\psi = 0, \tag{43}$$

where $\nu(X)$ is given by

$$\nu(X) = J\hat{h}_2'(X),$$
$$J = \frac{1}{\hat{h}_2}\left(2 - \frac{3}{4}\frac{\rho_2 h_1}{\rho_1\hat{h}_2 + \rho_2 h_1} + \frac{\rho_2\hat{h}_2}{\rho_1 h_1 + \rho_2\hat{h}_2} - \frac{2\rho_1\hat{h}_2^2}{\rho_1\hat{h}_2^2 - \rho_2 h_1^2}\right). \tag{44}$$

It is well known [10] that, when $\nu < 0$ in (44), a KdV solitary wave is disintegrated into a number of solitary waves. The number of solitary waves N to be disintegrated is determined by

$$N(N-1) \le \frac{2}{\mu} \le N(N+1) \tag{45}$$

where μ is given by

$$\mu = \left(\frac{\hat{h}_2}{h_2}\right)^{5/4}\left(\frac{\rho_1\hat{h}_2 + \rho_2 h_1}{\rho_1 h_2 + \rho_2 h_1}\right)^{3/4}\left(\frac{\rho_1 h_1 + \rho_2\hat{h}_2}{\rho_1 h_1 + \rho_2 h_2}\right)\frac{\left|\rho_1 h_2^2 - \rho_2 h_1^2\right|}{\left|\rho_1\hat{h}_2^2 - \rho_2 h_1^2\right|}, \tag{46}$$

and the final depth at $x = \infty$ is substituted for $\hat{h}_2$. As shown in Figure 11, depending on the depth and density ratios, the sign of J in (44) can be either positive or negative. Therefore, for $\nu < 0$, the bottom topography needs to vary upward ($\hat{h}_2'(x) < 0$) or downward ($\hat{h}_2'(x) > 0$).

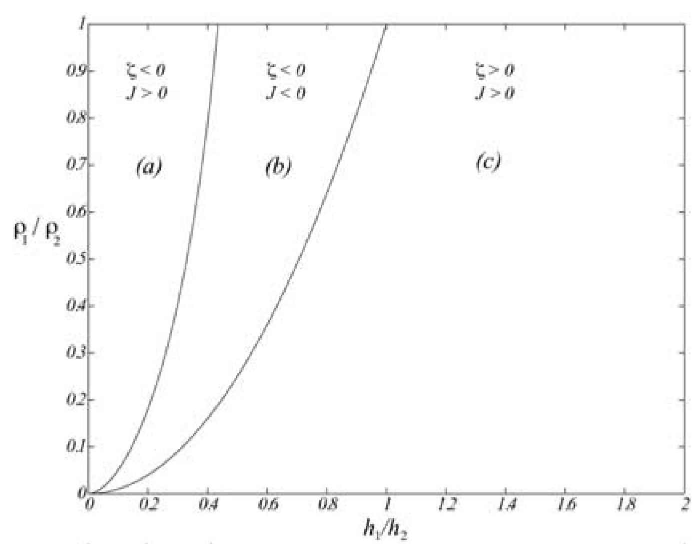

Figure 11. Condition of disintegration of a solitary wave propagating over non-uniform topography: (a) $h_2'(x) < 0$, (b) $h_2'(x) > 0$, (c) $h_2'(x) > 0$.

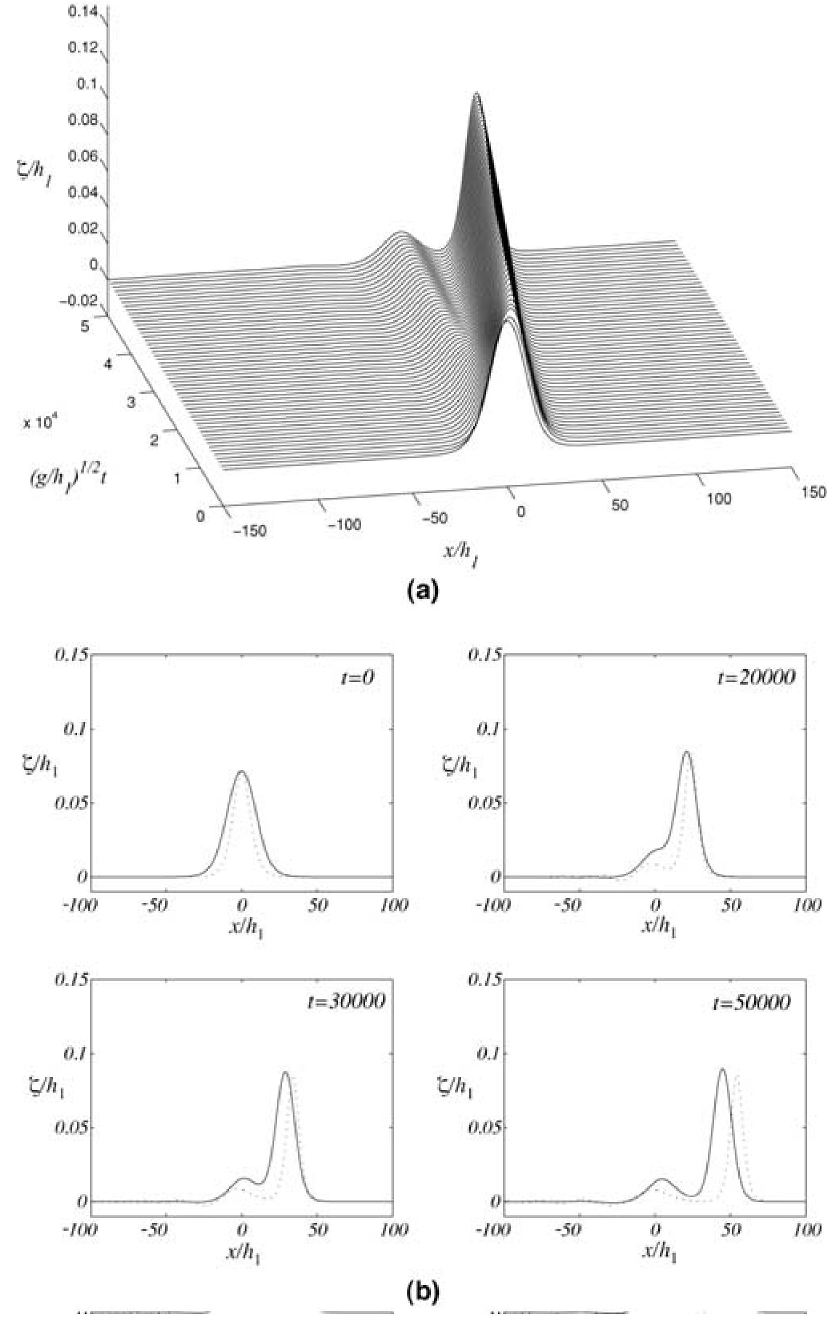

Figure 12. Transformation of a solitary wave of $a = 0.072$ climbing over a shelf, whose shape is given by (47) with $b_0 = 0.1$. The density and depth ratios are $\rho_2/\rho_1 = 1.01$ and $h_2/h_1 = 0.8$, respectively. (*a*) Numerical solutions of the strongly nonlinear model given by (1)–(3), (*b*) comparison of numerical solutions between the weakly and strongly nonlinear models with the same wave amplitude at $t = 0$, 20000, 30000, 50000.

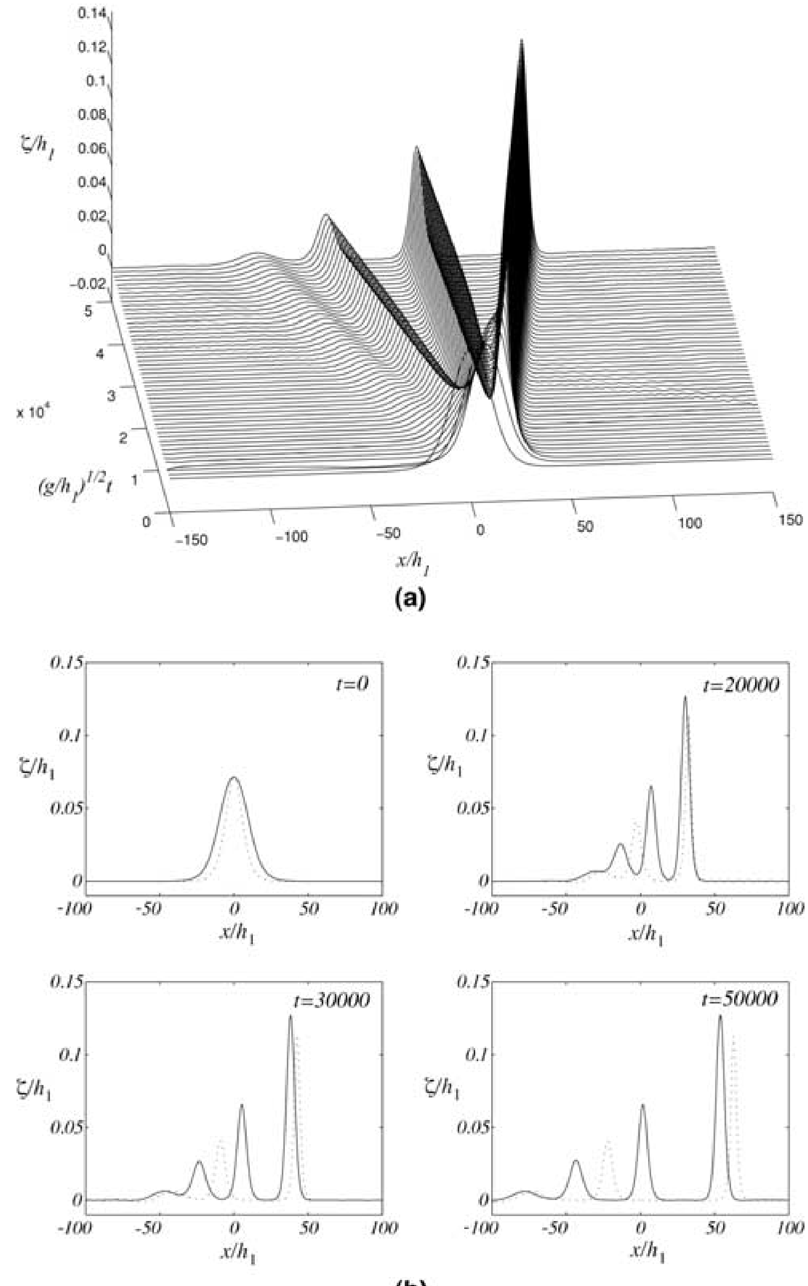

Figure 13. Transformation of a solitary wave of $a = 0.072$ climbing over a shelf, whose shape is given by (47) with $b_0 = 0.35$. The density and depth ratios are $\rho_2/\rho_1 = 1.01$ and $h_2/h_1 = 0.8$, respectively. (*a*) Numerical solutions of the strongly nonlinear model given by (1)–(3), (*b*) comparison of numerical solutions between the weakly and strongly nonlinear models with the same wave amplitude at $t = 0$, 20000, 30000, 50000.

To compare our numerical solutions of the strongly nonlinear model (1)–(3) with (45), we adopt the following bottom topography:

$$b(x) = \tfrac{1}{2} b_0 \tanh(x/10). \qquad (47)$$

For small $b_0\,(=0.1)$ (Figure 12), as predicted by (45), two solitary waves are generated from a single solitary wave of amplitude $a = 0.072$ and our numerical solutions of the strongly nonlinear model are close to those of the weakly nonlinear model (8)–(9). As b_0 increases, the weakly nonlinear prediction no longer remains valid. As shown in Figure 13, when $b_0 = 0.35$, numerical solutions of the strongly nonlinear model have generated four solitary waves while the weakly nonlinear analysis predicts only three solitary waves.

6. Conclusion

We have investigated the dynamics of large amplitude internal solitary waves by using a new strongly nonlinear model. The local stability analysis reveals that the model suffers the Kelvin–Helmholtz instability due to the presence of horizontal velocity jump across the interface induced by internal solitary wave. Even with simulations limited by this instability, we are able to demonstrate strong nonlinear effects on the interactions between large amplitude internal solitary waves. Our numerical solutions also show that the evolution of a large amplitude internal solitary wave over non-uniform topography is different from the weakly nonlinear prediction as wave amplitude increases. To improve the model and eliminate the instability, it might be crucial to take into consideration other physical effects such as viscosity, surface tension, or continuous stratification. For further validation of the model, it might be useful to compare our numerical solutions with exact solutions of the Euler system to be found numerically.

References

1. W. Choi and R. Camassa, Weakly nonlinear internal waves in a two-fluid system, *J. Fluid Mech.* 313:83–103 (1996).
2. T. P. Stanton and L. Ostrovsky, Observations of highly nonlinear internal solitons over the continental shelf, *Geophys. Res. Lett.* 25:2695–2698 (1998).
3. W. Choi and R. Camassa, Fully nonlinear internal waves in a two-fluid system, *J. Fluid Mech.* 396:1–36 (1999).
4. R. Camassa, W. Choi, H. Michallet, P. Rusas, and J. K. Sveen, Internal waves in two-layer fluids: An experimental, numerical and modeling investigation, *Preprint* (2001).
5. W. Choi, Modeling of strongly nonlinear internal waves in a multilayer system, *Proceedings of the Fourth Intl. Conf. on Hydrodynamics* (Y. Goda, M. Ikehata, and K. Suzuki, Eds.), Yokohama University, Japan, pp. 453–458, 2000.

6. P. G. Drazin and W. H. Reid, *Hydrodynamic Instability*, Cambridge University Press, New York, 1981.
7. G. B. Whitham, *Linear and Nonlinear Waves*, Wiley, New York, 1974.
8. T. Y. Wu, Bidirectional soliton street, *Acta Mechanica Sinica*, 11:289–306 (1995).
9. V. D. Djordjevic and L. G. Redekopp, On the development of packets of surface gravity waves moving over an even bottom, *Z. Angew. Math. Phys.* 29:950–962 (1978).
10. C. C. Mei, *The Applied Dynamics of Ocean Surface Waves*, World Scientific Publishing, Singapore, 1989.

Arizona State University
University of Michigan

(Received December 7, 2001)